Chapter - 7

Design and development of the $AgI/NiFe_2O_4$ Photo-Fenton Photocatalyst

7.1 Introduction

Fenton-like advanced oxidation processes (AOPs) have gained recognition as promising methods for the treatment of organic pollutants in different water sources [268,269]. Yet, both homogeneous and heterogeneous Fenton processes suffer from acidic pH range and recyclability issues[270]. The slow kinetics of conversion of the oxidized catalyst to its reduced state is the rate limiting step hampering catalyst reusability. Photo-Fenton processes, on the other hand, use light energy by photocatalysis to drive the reductive cleavage of H_2O_2 for hydroxyl radical generation[271]. In other words, the photo-excited electrons in the conduction band (CB) of the photocatalyst reduce H_2O_2 to generate hydroxyl radicals[272,273]. The photocatalysis cycle is completed by oxidation of molecules on the photo-excited holes of the valence band (VB). Separate oxidation and reduction centres in photo-Fenton photocatalysts avoid the rate limiting issues faced by normal Fenton processes.

Photocatalyst recovery and reuse is more economical if the material is superparamagnetic[274,275]. In this context, spinel nickel ferrite ($NiFe_2O_4$) nanoparticles, with a ~2.0 eV band gap, have a stable structure, elevated electrical resistivity, and remarkable photochemical stability[276,277]. Its magnetic properties arise from the anti-parallel spins of Ni^{2+} ions located at octahedral sites and Fe^{3+} ions situated at tetrahedral sites, contributing to a magnetic moment. Given the +3-oxidation state of Fe in $NiFe_2O_4$, the latter does not exhibit any dark Fenton activity[278]. But the moderate band gap and other attributes of pure $NiFe_2O_4$ mean it has the potential to serve as a reusable photocatalyst[90,279]. Nevertheless, $NiFe_2O_4$ suffers from poor photocatalytic efficiency because of the rapid recombination of photoexcited species[278]. The latter can be addressed by appropriate charge separation. A composite of $NiFe_2O_4$ and another photocatalytic component, with two parts having staggered VB and CB positions relative to one another, can enhance charge separation. The

two components will also have different adsorption properties that may help in execution of the target reaction.

Silver halides AgX (X = Cl, Br, I) are well-known for their photosensitivity and among them, AgI is a moderate band gap (~2.7 eV) semiconductor with promising photocatalytic capability. Nonetheless, the practical applicability of AgI is limited by its larger particle sizes and lower photostability[280]. Contrary to the foregoing, composites of AgI with other semiconductors have substantially improved photostability and photocatalytic activity due to enhanced charge separation. For instance, the AgI composites like AgI/UIO-66, Fe_3O_4/rGO/AgI, $CuWO_4$/AgI, and $ZnFe_2O_4$/AgI etc. have demonstrated significant photocatalytic activity under visible light for the degradation of various pollutants[280–283]. Given, the advantages stated above, and the staggered band positions of AgI relative to that of $NiFe_2O_4$, the present research investigates the photo-Fenton activity of AgI/$NiFe_2O_4$ composites. Note that there is no previous report in the literature on the photo-Fenton activity of this composite.

An efficient photo-Fenton photocatalyst (in its photo-excited state) will effectively activate of the HO-OH bond (in H_2O_2) for efficient hydroxyl radical production, also discussed in previous chapter 6. Hence, before embarking on an extensive experimental investigation, it was decided to investigate by appropriate DFT calculations the feasibility of the AgI/$NiFe_2O_4$ composite acting as a photo-Fenton photocatalyst for efficient production of hydroxyl radicals. A few combined experimental and computational studies have demonstrated that design of an effective photocatalyst necessitates that its photo-excited highest occupied molecular orbital (HOMO) location (or the CB) should interact more favourably with species to be reduced[80]. The latter corresponds to photo-excited electrons in the CB of the photocatalyst reducing H_2O_2 to generate hydroxyl radicals. This premise is a primary criterion for the screening of a photo-Fenton catalyst. Thus, in the first

part of this investigation, we undertook density functional theory (DFT) and time-dependent DFT (TD-DFT) calculations to investigate whether the AgI/$NiFe_2O_4$ composite fulfils the above-mentioned criteria. Our DFT and TD-DFT investigations revealed that the model of the AgI/$NiFe_2O_4$ composite fulfils this requirement.

Following this, magnetically separable AgI/$NiFe_2O_4$ nanocomposites with varying AgI contents were synthesized using a straightforward hydrothermal and co-precipitation method. The AgI/$NiFe_2O_4$ composites were evaluated for their photo-Fenton tetracycline (TC) degradation activity. The target tetracycline (TC) is an antibiotic that has been extensively used in agriculture, animal treatment, and human therapy[284,285]. Diverse waterways, including surface water, groundwater, and even potable water, have been found to contain TC. The presence of the partially metabolized and unmetabolized antibiotic makes the target microbes resistant to it [243,286,287]. Consequently, environmental regulatory agencies have made the elimination of TC from aquatic sources compulsory. Conventional wastewater treatment methods cannot adequately eliminate TC due to its robust chemical composition and resistance to biodegradation[287,288].

The AgI/$NiFe_2O_4$ composites prepared were subjected to characterization using X-ray diffraction (XRD), transmission electron microscopy (TEM), scanning electron microscopy (SEM), X-ray photoelectron spectroscopy (XPS), vibrating sample magnetometry (VSM), and UV–vis diffuse reflectance spectra (DRS). As mentioned earlier, DFT and TD-DFT calculations were carried out on a model of the AgI/$NiFe_2O_4$ composite to investigate H_2O_2 interaction with its parts. Natural bond analysis (NBO) was also performed on the optimized model to examine the charge transfer between H_2O_2, AgI, and $NiFe_2O_4$. Finally, the experimental, DFT, and TD-DFT results were integrated to propose a photo-Fenton mechanism.

7.2 Experimental section

The precursor materials $Ni(NO_3)_2$, $Fe(NO_3)_3.9H_2O$, NaOH, $AgNO_3$, and KI were procured from Merck and utilized without additional purification. All chemicals employed were of analytical reagent (AR) grade. Double distilled water (DW) served as the solvent for all reactions.

7.2.1 Synthesis of $NiFe_2O_4$ nanoparticles

The procedure for synthesis of $NiFe_2O_4$ using hydrothermal method, has been discussed in section 4.2.1 of chapter 4.

7.2.2 Synthesis of AgI/ $NiFe_2O_4$ nanoparticles

A fixed amount (135 mg) of $NiFe_2O_4$ nanoparticles was first dispersed in 50 ml DW by prolonged bath sonication. Then 0.064 mmol of $AgNO_3$ was added to the re-dispersed $NiFe_2O_4$ suspension. The resulting mixture was agitated on a thermostatic shaker for 24 hours to ensure Ag^+ ion adsorption on $NiFe_2O_4$ nanostructures. After another 4 hours of steady stirring, 50 ml of KI solution (amounting to 0.064 mmol) was added dropwise to the dispersion. The (light brown) precipitate produced was washed multiple times with DW and ethanol. The finished product underwent drying at 60°C. The nanocomposite sample obtained was 10 weight percent AgI loaded (or precipitated) on $NiFe_2O_4$ nanoparticles. This composite sample was designated as 10AgINIF. Additionally, two more composite samples with 30 and 50% AgI loadings on $NiFe_2O_4$ were prepared and labelled as 30AgINIF and 50AgINIF, respectively.

7.2.3 Fenton activity of the nanocomposites

All the prepared samples were initially examined for Fenton activity towards TC degradation (under the dark condition). Negligible TC degradation was observed under

these conditions.

The experimental conditions for assessing the Fenton activities of the composites in the absence of visible light irradiation were identical to those detailed in the next section.

7.2.4 Photo-Fenton catalytic activity

The photo-Fenton activities of the synthesized catalysts were evaluated for TC degradation under cool white 14W LED illumination (Intensity: 1430 W/m^2). Typically, 2 mg of each prepared photocatalyst was dispersed in 2 ml of DW via sonication for 20 minutes. Each experiment entailed adding 100 µL of catalyst suspension to a 10 ppm TC aqueous solution (3 ml volume) in a 3.5 ml quartz cuvette. The resulting mixture was kept in darkness for 45 minutes to establish adsorption-desorption equilibrium. Subsequently, an appropriate quantity of H_2O_2 was added to the mixture. Following this step, the mixture was exposed to visible light. The absorption spectra of TC degradation were monitored after separating the photocatalyst magnetically at regular intervals. Several experiments were carried out under various controlled conditions. Initially, experiments were conducted at different pH levels to ascertain the optimal reaction pH. Additionally, the amount of H_2O_2 also influences the photo-Fenton activity. Excess H_2O_2 can scavenge hydroxyl radicals. Thus, the photo-Fenton activity of the AgINIF composite was assessed at different amounts of H_2O_2. Finally, the composite demonstrating the best photo-Fenton activity among the three AgINIF photocatalyst was evaluated at the optimum pH and H_2O_2 conditions. This photo Fenton experiment was also performed with scavenger molecules specific to $OH^{\cdot}$, and h^+ reactive species. Isopropanol (IPA), and Ethylene diamine tetra acetic acid (EDTA) were the scavengers for trapping the $OH^{\cdot}$, and h^+ active species, respectively. In the active species determination experiment, 100uL of 0.185 mM IPA or 0.5 mM EDTA was added to the reaction mixture. The rest of the experimental procedure remained the same. All the photo Fenton degradation experiments were conducted at 27°C temperature.

7.2.5 DFT calculations

DFT calculations were performed to understand the role of composite formation on photo Fenton degradation activity. The unit cell of $NiFe_2O_4$ (MP-22684) was obtained from the material project database. The unit cell of $NiFe_2O_4$ (MP-22684) was multiplied to build a $3 \times 3 \times 3$ supercell by Materials and Process Simulation (MAPS) version 4.4 software (released by Scienomics)[82,216]. A small cluster of $NiFe_2O_4$ having 30 atoms was cleaved from its supercell using the MAPS 4.4 software. This cluster is abbreviated as NIF for further DFT calculations. Similarly, the unit cell of AgI (MP-22894) was obtained from material project database[216]. Then, a small AgI cluster (having 5 atoms) was cleaved from its $3 \times 3 \times 3$ supercell by using the MAPS software. We denote this AgI cluster by the AgI5 abbreviation for all DFT calculations. All molecular models (including H_2O_2) were constructed on the GaussView 6.0 software. The optimizations and energy calculations of clusters and molecular models in this study were accomplished using the Gaussian 16 software. The B3LYP (Becke-3-Parameter-Lee-Yang-Parr) functional was used for all DFT and TD-DFT calculations. The DGDZVP basis set was used for the structure optimization of the NIF and AgI5 clusters. The H_2O_2 was optimized using the 6-311g basis set[289]. Figure 7.1 shows the optimized structures of H_2O_2, NIF and AgI5 entities.

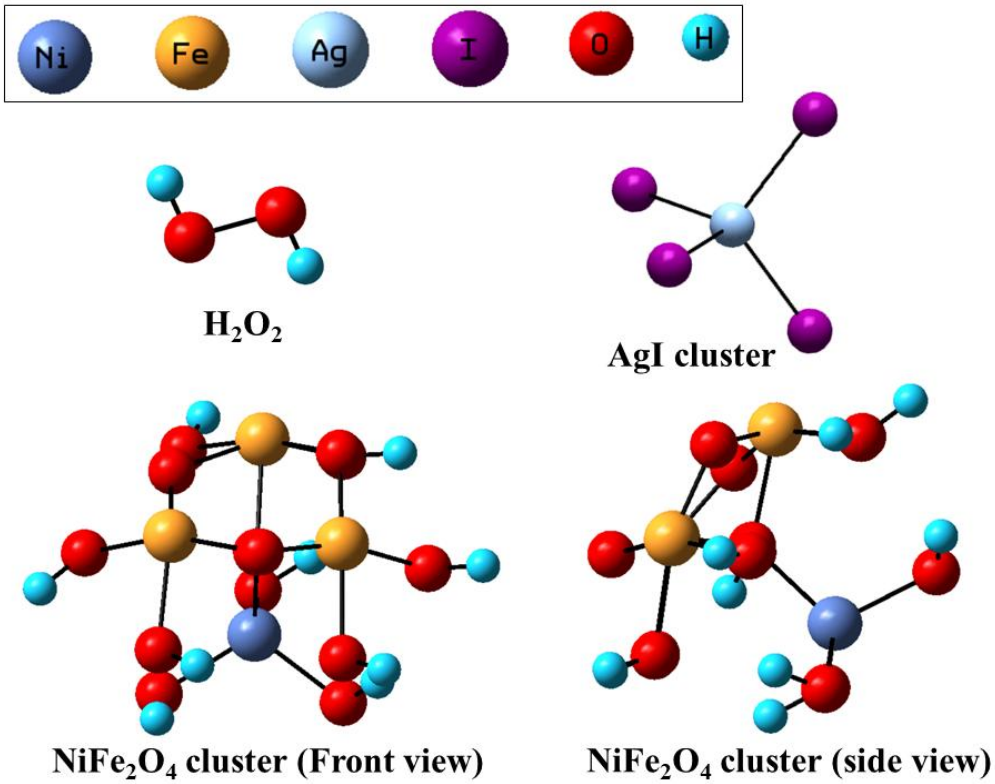

Figure 7.1. Optimized structure of H_2O_2, AgI cluster and $NiFe_2O_4$ cluster.

The NIF cluster was placed near to AgI5 molecule in various orientations to obtain the optimized structure of the NIF/AgI5 composite. These alignments were selected such that the iodine of AgI5 pointed towards Fe in the NIF cluster. Furthermore, the surface oxygens of the NIF part having incomplete coordination were passivated by attaching hydrogen atoms to them. Similarly, in the case of AgI, two water molecules were placed to passivate the AgI surface not adjacent to the NIF cluster. Geometry optimization DFT calculations were run on all possible arrangements to find the composite model with the lowest energy. These calculations used a DGDZVP basis set for all atoms (except O, and H atoms) under the B3LYP functional. For O, and H atoms, 6-311g basis was used under the same functional. Figure 7.2 displays the geometry of the optimized (lowest energy) composite model abbreviated as the NIF30_AgI5 system.

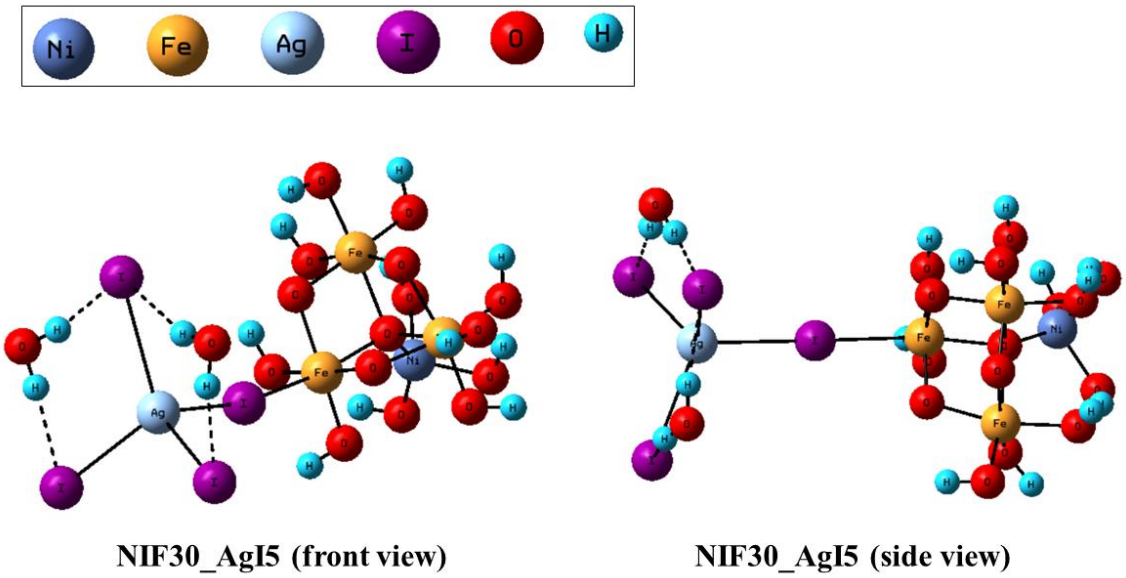

Figure 7.2 The optimized structure of the NIF30_AgI5 system.

Two separate DFT calculations (gas phase) were carried out to investigate the interaction of H_2O_2 with the NIF and the AgI5 part of the ground state NIF30_AgI5 system. Natural bond orbital (NBO) analysis was also performed to quantify the charge transfer from donor to acceptor orbitals.

7.2.6 TD-DFT calculations

Excited state TDDFT calculations were used to simulate the gas phase UV-visible spectrum of the NIF30_AgI5 model[290]. All TDDFT calculations were conducted at the same level of theory as the ground state calculations. The HOMO and LUMO locations in the composite model corresponding to the most intense UV-visible absorption line were calculated. Separate DFT calculations (gas phase) were carried out to investigate the interaction of H_2O_2 with the excited state HOMO and LUMO locations of the NIF30_AgI5 model.

7.3 Results and Discussion

7.3.1 Material characterizations

Figure 7.3 shows the XRD patterns of pure AgI, pure $NiFe_2O_4$ and as-prepared AgI/$NiFe_2O_4$ (10AgINIF, 30AgINIF, and 50AgINIF) nanocomposites with different weight % of AgI loading. The XRD pattern of the $NiFe_2O_4$ powder sample at 18.4°, 30.2°, 35.7°, 37.3°, 43.3°, 53.8°, 57.2°, 62.9° and 74.4° (2θ) were corresponding to the (111), (220), (311), (222), (400), (422), (511), (440), and (533) planes of FCC (inverse spinel) lattice of $NiFe_2O_4$ (JCPDS file number 74-2081). Similarly, the peaks at 23.71°, 39.25° and 46.24° in the AgI XRD pattern were indexed to the (111), (220) and (311) planes of the AgI FCC (JCPDS file number 78-0641). The peaks in the diffraction patterns of the prepared nanocomposites correspond to FCC AgI and FCC $NiFe_2O_4$. The relative intensity of the peaks at 23.71°, 39.25° and 46.24° increased with the AgI content. No impurity peaks were observed in the XRD diffraction patterns of composites, confirming the successful preparation of the intended AgI/$NiFe_2O_4$ composites.

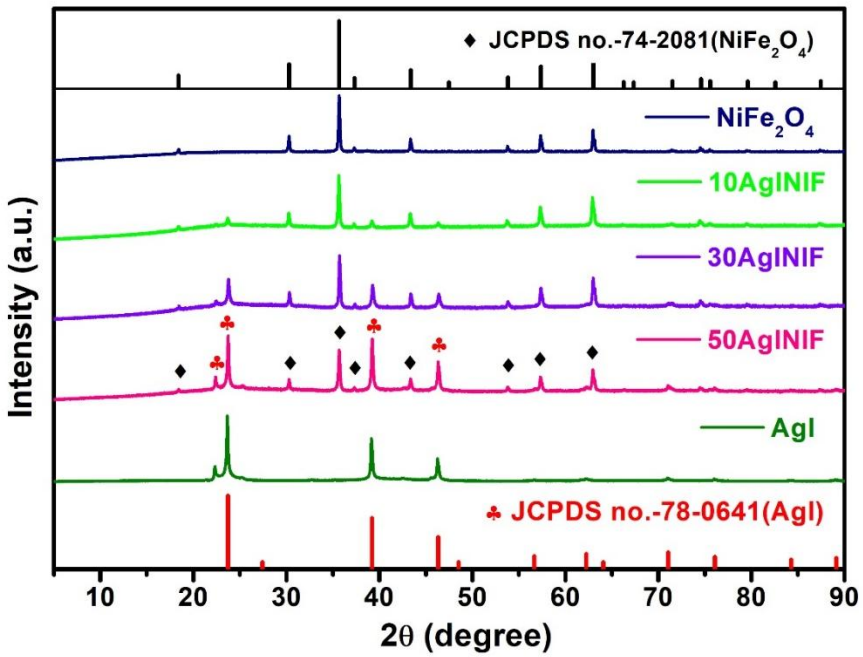

Figure 7.3 XRD pattern of pure AgI, pure $NiFe_2O_4$ and their nanocomposites.

As is reported later, among the materials prepared in this study, the 30AgINIF nanocomposite sample exhibited the best photo-Fenton activity for TC degradation. Hence,

TEM and SEM images of only the 30AgINIF nanocomposite were analysed. Figure 7.4a shows that most $NiFe_2O_4$ particles have octahedral morphology. The corresponding HR-TEM (Figure 7.4b) demonstrates a lattice fringe with an interplanar spacing of ~0.294nm, corresponding to the (220) plane of FCC $NiFe_2O_4$. Figure 7.4c shows octahedral $NiFe_2O_4$ particles in close contact with irregularly shaped AgI particles, indicating the formation of a heterojunction. The HR-TEM (Figure 7.4d) of the same sample shows two adjacent regions having lattice fringes of 0.374 nm and 0.294 nm spacing. These correspond to the AgI (111) and $NiFe_2O_4$ (220) planes, respectively. The adjacent placing of AgI and $NiFe_2O_4$ parts confirm the formation of a composite.

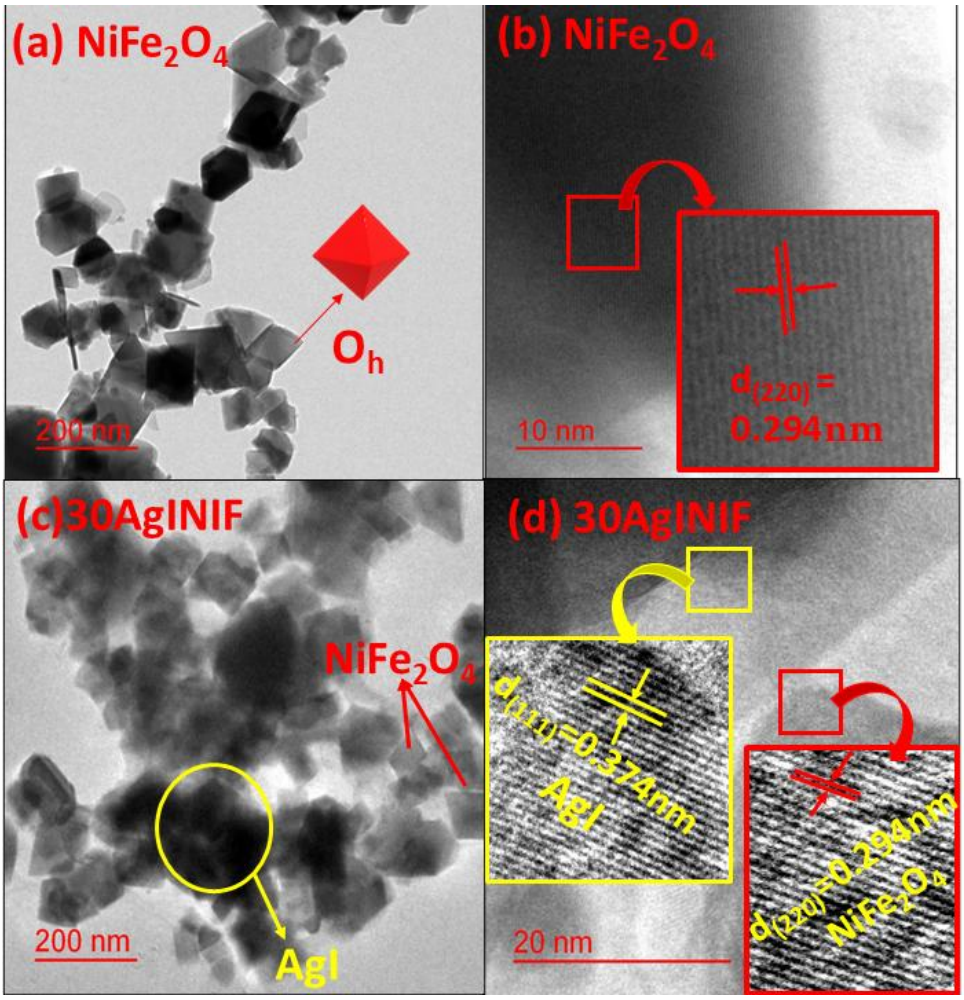

Figure 7.4 TEM of (a) $NiFe_2O_4$, (c) 30AgINIF, and HR-TEM of (b) $NiFe_2O_4$, (d) 30AgINIF samples.

Figure 7.5a displays a typical SEM micrograph of the 30AgINIF nanocomposite sample. It shows the octahedral $NiFe_2O_4$ particles surrounded by irregularly shaped AgI nanoparticles. The corresponding elemental distribution profile of 30AgINIF (Figure 7.5b) exhibits AgI containing particles adjacent to $NiFe_2O_4$ compositions, another confirmation of AgI/$NiFe_2O_4$ composite formation.

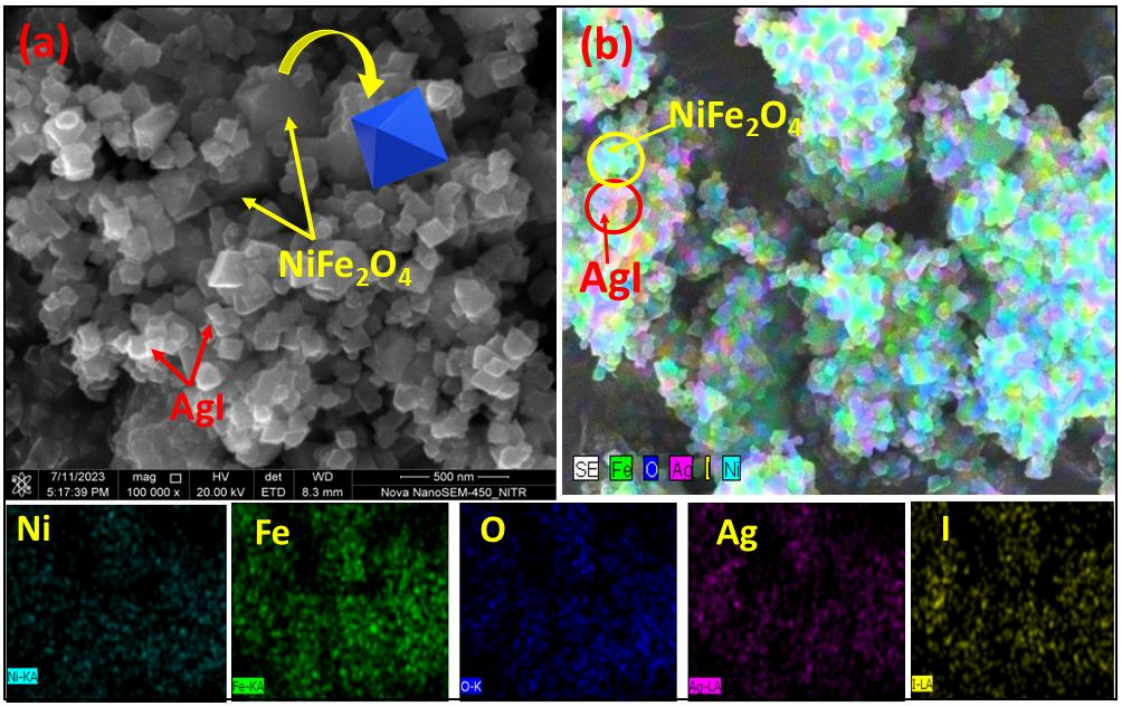

Figure 7.5 (a) SEM images (b) Elemental distribution profile of 30AgINIF sample.

XPS was used to determine the elements present and their chemical states in $NiFe_2O_4$, AgI, and 30AgINIF composite (Figure 7.6) samples. The XPS spectrum of Ag3d of pure AgI, displays the $Ag3d_{5/2}$ and $Ag3d_{3/2}$ at 367.39 and 373.39 eV binding energies (Figure 7.6a). These peaks shift to slightly higher binding energies at 367.84 and 373.82 eV in the XPS of the (30AgINIF) composite. Similarly, the two $I3d_{5/2}$ and $I3d_{3/2}$ peaks (in the AgI spectrum) appearing at 619.81 and 631.27 eV shift to greater values of 619.90 and 631.41 eV in the spectrum of the composite (Figure 7.6b).

Figure 7.6c shows the Ni2p part of $NiFe_2O_4$ XPS spectrum. It displays the $Ni2p_{3/2}$ and $Ni2p_{1/2}$ peaks at 854.95 and 873.01 eV binding energies after appropriate curve fitting. These peaks shift to slightly lower binding energies in the 30AgINIF composite (Figure 7.6c) XPS spectrum. The spectra confirm that Ni is in the +2 oxidation state in both $NiFe_2O_4$ and the 30AgINIF composite. These spectra also display two shake-up satellite peaks at ~861.51 and ~879.98 eV in $NiFe_2O_4$ and the composite. Figure 7.6d gives the Fe2p part of the XPS spectra of $NiFe_2O_4$ and the 30AgINIF composite. The HR XPS spectrum of Fe2p of $NiFe_2O_4$ display the four characteristic peaks at 710.0, 712.19, and 723.69, 726.0 eV binding energies, respectively. Additionally, two shake up satellite peaks were observed at 718.42 ($Fe2p_{3/2}$), and 733.83 eV ($Fe2p_{1/2}$) due to Fe^{3+} in the $NiFe_2O_4$. The difference of binding energy of $Fe2p_{3/2}$ main peak and $Fe2p_{3/2}$ satellite peak is ~8.0 eV[196]. Satellite peaks and their distance from the Fe2p peak enables the classification and assignment of the HR-XPS deconvoluted peaks in the Fe2p region. The presence of satellite peaks at a specified distance range from the Fe2p peak indicates only Fe^{3+} is present in the $NiFe_2O_4$ sample[196]. Using the above reasoning, it was inferred that the binding energies at 710.68 ($Fe2p_{3/2}$), and 723.88 eV ($Fe2p_{1/2}$) correspond to Fe in +3 oxidation state present in octahedral sites[82,197]. The binding energies at 712.57 (Fe2p3/2), and 725.43 eV (Fe2p1/2) correspond to Fe in +3 oxidation state in tetrahedral sites[197]. The same set of peaks are observed in the Fe2p part of XPS spectrum of the 30AgINIF composite sample. The peaks show a shift to slightly lower binding energies at 709.91, 712.05 and 723.2, 724.84 eV. The binding energies at 709.91 ($Fe2p_{3/2}$), and 723.2 eV ($Fe2p_{1/2}$) correspond to Fe in +3 oxidation state present in octahedral sites. The binding energies at 712.05 ($Fe2p_{3/2}$), and 724.84 eV ($Fe2p_{1/2}$) correspond to Fe in +3 oxidation state present in tetrahedral sites. Further, two shake up satellite peaks were observed at 718.39 ($Fe2p_{3/2}$), and 733.08 eV ($Fe2p_{1/2}$) due to Fe^{3+} in the $NiFe_2O_4$.

Figure 7.6e depicts the XPS spectrum of O1s in pure $NiFe_2O_4$ and 30AgINIF composite. The curve fitting of the O1s part of the pure $NiFe_2O_4$ spectrum yielded three peaks at 529.7, 531.0, and 532.18 eV. These correspond to lattice oxygen (OL), oxygen vacancy (OV), and chemisorbed oxygen (OH), respectively. In comparison to pure $NiFe_2O_4$, the characteristic peaks of the O1s spectra of 30AgINIF were substantially altered because of chemical coupling between $NiFe_2O_4$ and AgI. All three peaks of O1s spectra shift towards slightly higher binding energies at 530.2, 531.4, and 532.3 eV, respectively. The change of peak intensity and position at the lattice oxygen peak (530.2 eV) may be attributed to the formation of new metal- oxygen bonds[291]. Meanwhile, the peaks at 531.4 eV and 532.3 eV were related to the oxygen vacancy (OV), and chemisorbed oxygen (OH), respectively. Overall, the XPS observations tell us that composite formation causes charge transfer from the AgI side to the $NiFe_2O_4$ part. Thus, the AgI and $NiFe_2O_4$ parts of the composite are chemically bound.

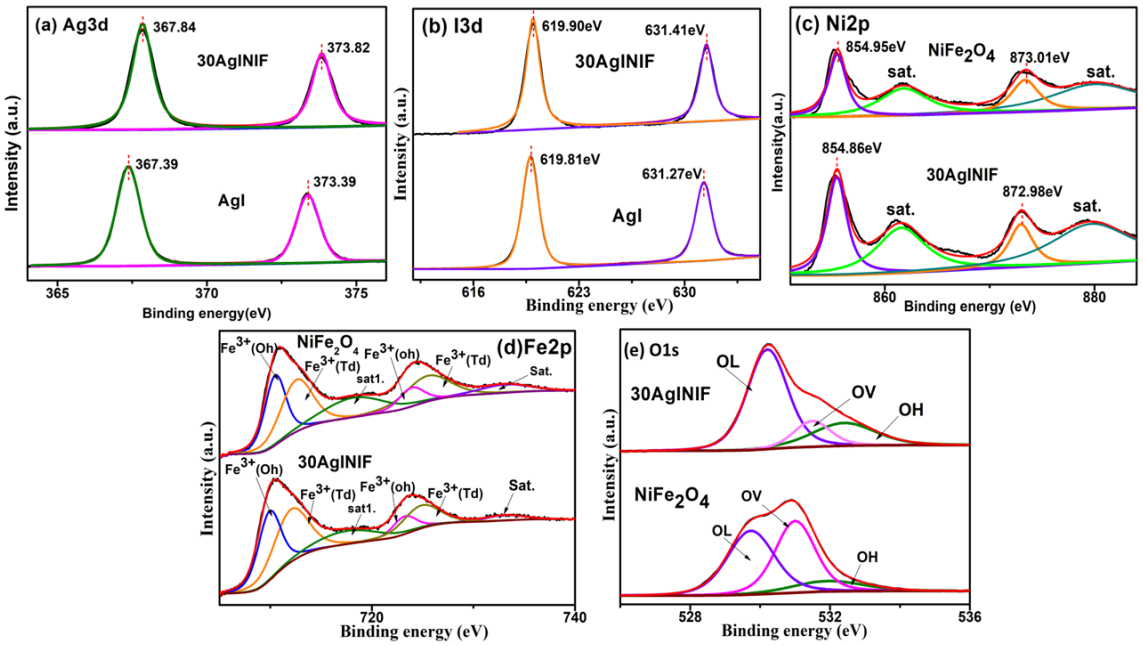

Figure 7.6 A comparison of the deconvoluted (a) Ag3d, (b) I3d parts of the pure AgI and 30AgINIF composite XPS spectra. A comparison of the (c) Ni2p, (d) Fe2p, and (e) O1s regions of XPS spectra of pure $NiFe_2O_4$, and 30AgINIF composite.

Figure 7.7 illustrates the magnetization versus magnetic field (M-H) curves for both the $NiFe_2O_4$ and 30AgINIF samples. The presence of hysteresis loops with negligible coercivity and remanence indicates that the samples demonstrate superparamagnetic behavior. The saturation magnetization (Ms) values were determined to be 39.86 emu/g for pure $NiFe_2O_4$ and 16.08 emu/g for 30AgINIF nanocomposite, respectively. The decreased Ms value observed in the 30AgINIF sample is likely due to the inclusion of non-magnetic AgI nanoparticles within the composite. Magnetic separation of the 30AgINIF sample was demonstrated by positioning a bar magnet near the cuvette containing the TC solution of photocatalysts. The inset image in Figure 7.7a distinctly depicts that 30AgINIF nanoparticles can be readily isolated by the applying an external magnetic field.

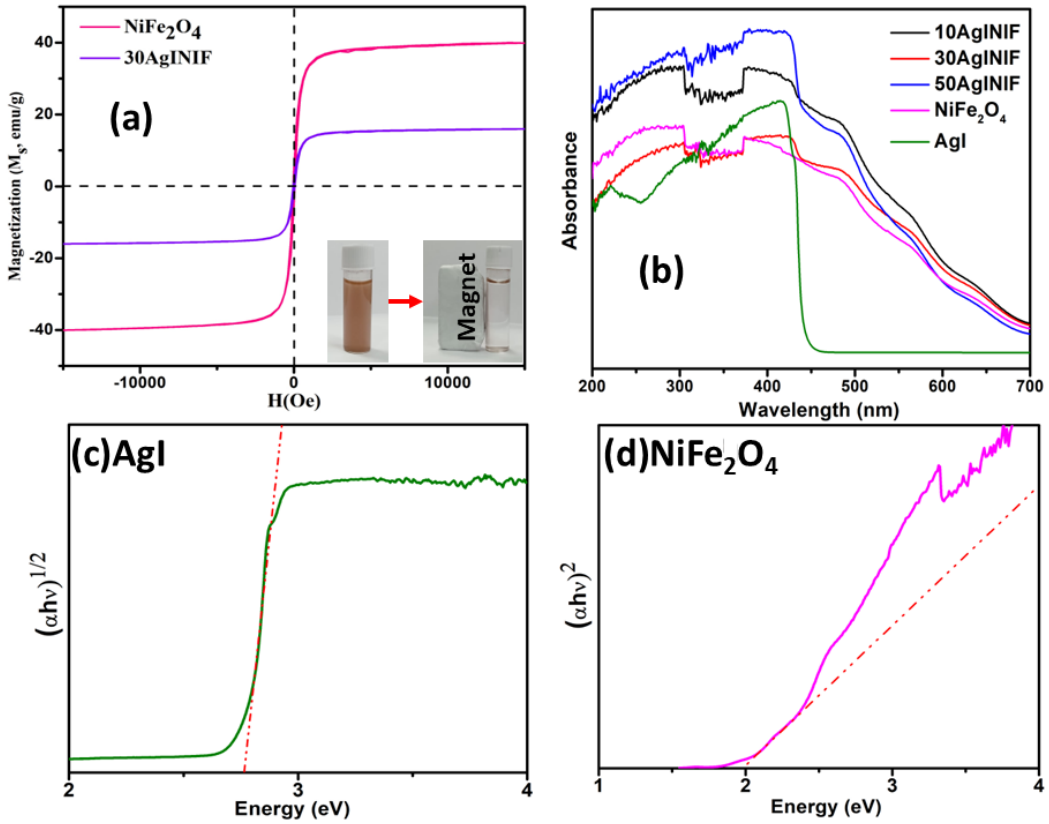

Figure 7.7 (a) VSM plots of pure $NiFe_2O_4$ and 30AgINIF samples, (b) UV-DRS spectra of pure AgI, pure $NiFe_2O_4$ and their composites, the Tauc plots of (c) pure AgI, (d) pure $NiFe_2O_4$.

Figure 7.7b displays the solid-state UV-vis absorption spectra of pure AgI, $NiFe_2O_4$, and their respective nanocomposites prepared in this study. Figures 7.7c and 7.7d present the Tauc plots for AgI and $NiFe_2O_4$. The Tauc equations, represented as $(\alpha h\nu)^{1/n}$ versus photon energy ($h\nu$), were utilized to determine the band gaps of bare AgI and $NiFe_2O_4$. The symbols 'α', '*h*', and 'υ' are referred to as absorption coefficient, Planck's constant, and photon frequency in the Tauc relation. For direct transition, n equals 1/2, and 2 for indirect transitions[292]. From the Tauc equations the calculated band gaps (E_g) of $NiFe_2O_4$ (E_g) and AgI are 1.98 eV (direct) and 2.77 eV (indirect).

MS data were acquired at 500Hz to validate the semiconductor type and to calculate the band edge positions of AgI and $NiFe_2O_4$ semiconductors. The equation V(NHE) = V(Ag/AgCl) + 0.059 pH + 0.197 was utilized to establish the potential (V) versus the normal hydrogen electrode (NHE) scale for the MS plots[135]. The pH of the electrolyte was ~7.2. Figures 7.8a and 7.8b displays the MS plots of pure AgI and $NiFe_2O_4$ semiconductor components. Both AgI and $NiFe_2O_4$ are n-type semiconductors since they both have a positive slope in MS plots[293]. The CB edge potentials for AgI and $NiFe_2O_4$ are -0.57 and -0.71 V, respectively. Using these CB edge values, the VB edges of the AgI and $NiFe_2O_4$ were determined by the equation $E_g = E_{VB} - E_{CB}$. The VB edge is 2.2 V for AgI and 1.28 V for $NiFe_2O_4$. This result confirms that the band positions of the two components (AgI and $NiFe_2O_4$) of the composite (AgINIF) are staggered with respect to each other.

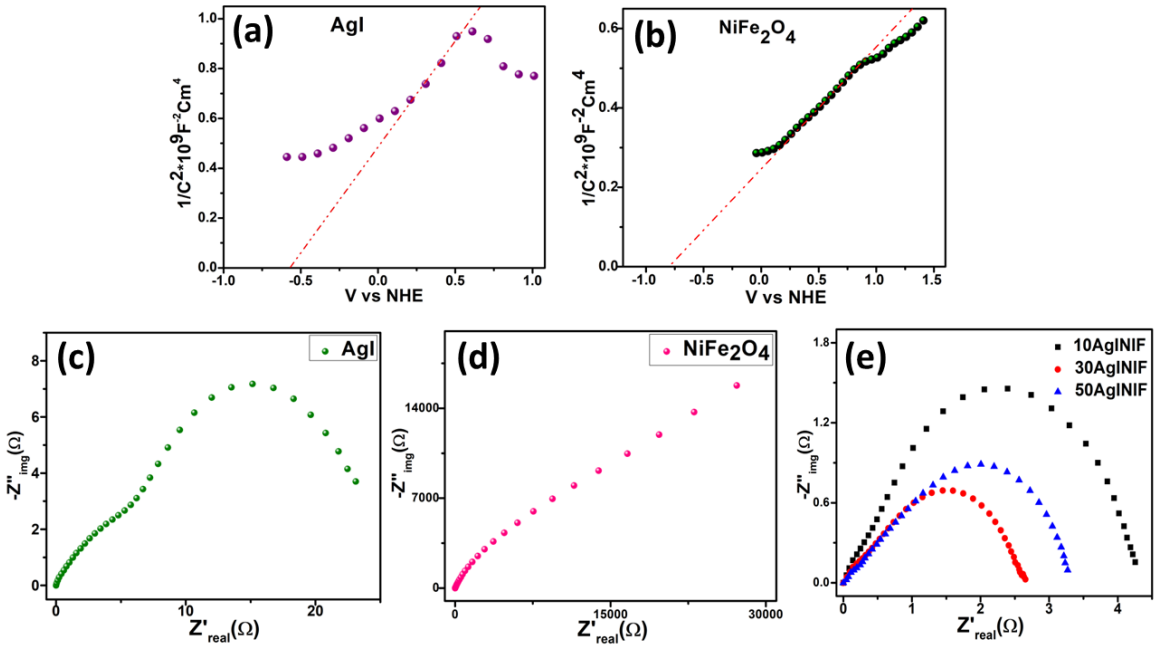

Figure 7.8 Mott Schottky plots of (a) AgI, and (b) $NiFe_2O_4$ samples, Nyquist plot for (c) AgI, (d) $NiFe_2O_4$, and (e) their nanocomposites.

The charge separation and migration caused by light is an important element in photocatalytic processes. The electrochemical impedance spectroscopy (EIS) method is employed to assess the efficiency of electron-hole pair separation[294]. The charge-transfer resistance is directly proportional to the diameter of the semicircle illustrated in the plot. Figures 7.8(c-e) depict the Nyquist impedance spectra of pristine AgI, pristine $NiFe_2O_4$ and their composites (10AgINIF, 30AgINIF, and 50AgINIF) photocatalysts. The 30AgINIF nanocomposite demonstrated the smallest semicircle, implying the lowest charge transfer resistance. This shows that the constructed $NiFe_2O_4$-AgI heterostructure has dramatically increased electron/hole separation and charge transfer efficiency, both of which are advantageous in photocatalysis.

7.3.2 Photocatalysis investigations

The photo-Fenton activities of pure $NiFe_2O_4$, AgI, and their composites (10AgINIF, 30AgINIF, and 50AgINIF) for TC degradation have been investigated. The photo-Fenton activity of the 30AgINIF nanocomposite for TC degradation was examined at three different pH values (1, 3, and 7). Figure 7.9a shows that the 30AgINIF composite exhibits the best photo-Fenton activity for TC degradation at acidic pH 3.

The amount of H_2O_2 is a critical aspect of photo-Fenton reaction kinetics optimization. A set of experiments were carried out on 30AgiNIF at pH 3 using different volumes of H_2O_2 (50 µL, 100 µL, and 150 µL) from a 0.5M H_2O_2 stock solution to find the H_2O_2 amount required for optimum photo-Fenton activity. Figure 7.9b shows that the experiment with 100µL of H_2O_2 demonstrated nearly complete (~100%) degradation of TC within 100 minutes of the photo-Fenton reaction. Hence, rest of the photo-Fenton reactions were carried out using 100 µL of 0.5M H_2O_2. Besides 100 µL 0.5 M H_2O_2, all photo-Fenton degradation experiments contained 3 ml of 10 ppm tetracycline and 100 µL of 1mg/ml of the catalyst suspension. The final volume of the reaction mixture was 3.2 ml. Figure 7.9c displays the UV–visible absorbance spectra of TC degradation by 30AgINIF nanoparticles. The intensity of the UV-visible absorbance decreased uniformly to nearly zero without showing the formation of any additional or new peak. The foregoing indicates that tetracycline degraded to small aliphatic fragments which do not have any UV-visible signature. Nearly all (~100%) of TC was degraded within 100 minutes of exposure to visible light. Note that the degradation efficiency decreased on further increase in the amount of H_2O_2. Excess H_2O_2 acts as ·OH radical scavenger to generate the hydroperoxyl radical ($\bullet HO_2$), a weaker oxidizing agent than ·OH radical [295]. Additionally, Figure 7.9d compares the photo-Fenton activities of the physical blending mixture of 30% AgI and 70% $NiFe_2O_4$ photocatalyst and the 30AgINiF composite sample. Under these conditions, only 27% tetracycline photo-Fenton degradation was observed in 100 minutes reaction time.

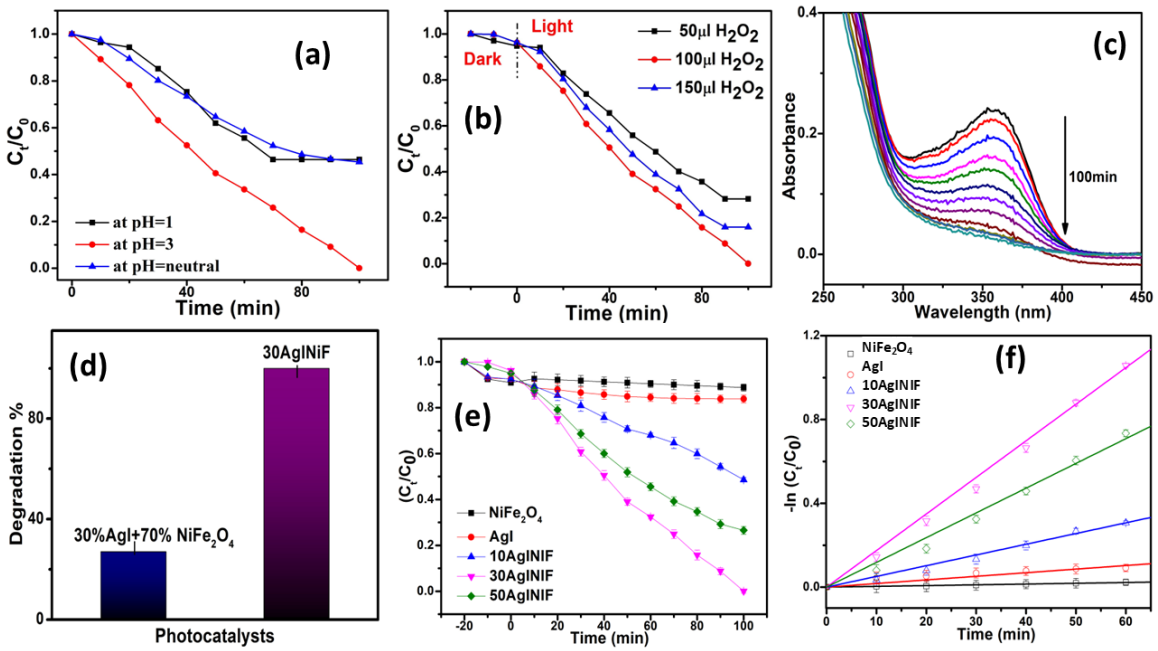

Figure 7.9 (a) Effect of pH on photo-Fenton degradation of TC on 30AgINIF catalyst, (b) Effect of H_2O_2 amount on photo-Fenton degradation of TC on 30AgINIF catalyst, (c) UV-Visible absorbance spectra of degradation of Tetracycline (TC) by 30AgINIF composite, (d) % photo-Fenton degradation of TC by physical blending mixture of 30% AgI and 70% $NiFe_2O_4$ photocatalyst and the 30AgINIF photocatalyst, (e) Comparison plot of photo-Fenton TC degradation activity of pure AgI, pure $NiFe_2O_4$, and their composites, and (f) Linear plot of pseudo-first order kinetics of different catalyst.

Figure 7.9e presents a comparison plot of photo-Fenton TC degradation for all the prepared samples in this study (pH~3 using 100 µL of 0.5M H_2O_2). Nanocomposite samples exhibit better photo-Fenton activities than pure $NiFe_2O_4$ and AgI. Furthermore, among the nanocomposites, 30AgINIF demonstrates the best photo-Fenton activity. Figure 7.9f illustrates that photo-Fenton TC degradation on these nanocomposites follow pseudo-first-order kinetics. The comparison graph of first order rate constant for pure AgI, pure $NiFe_2O_4$, their composites is shown in Figure 7.12c. The figure shows that the rate constant is highest for 30AgINIF photocatalyst among all the photocatalysts used for TC degradation. This further proves that 30AgINIF photocatalyst has best photocatalytic degradation efficiency

for TC degradation. Table 7.1 compares the photo-Fenton TC degradation activity on 30AgINIF with previous research work in terms of their turnover frequency (TOF) values. The rate constants of reactions with different orders are not comparable and cannot be used as a measure of photo-Fenton activity of the photocatalyst. Moreover, rate constants do not account for photocatalyst amount. Accordingly, we calculated the TOF values of photo-Fenton TC degradation on 30AgINIF and compared it with the results of other photo-Fenton studies published in the literature. Note that the TOF values for the studies published earlier in the literature were calculated from the data available in these publications.

The fourth column of Table 7.1 introduces H_2O_2 normalized TOF values (abbreviated as HTOF). Here, the TOF values are divided by the amount of H_2O_2 used in the reaction. The amount of H_2O_2 determines the cost of upscaling a process to practical or industrial levels. Hence, HTOF values project a vital practical aspect of the process. Both TOF and HTOF values of photo-Fenton TC degradation on 30AgINIF are higher than other values in Table 7.1. Thus, the photo-Fenton TC degradation activity of 30AgINIF is significantly higher than other publications considered in this Table.

Table 7.1 Efficiency Comparison data of 30AgINIF and other reported catalyst for TC degradation under photo-Fenton condition. (Note- The TOF and H_2O_2 normalized TOF for the reported photocatalyst have been calculated using experiment data provided in referred publications.)

Catalyst	Working Conditions	Degradation efficiency	TOF (μmol g^{-1} h^{-1})	H_2O_2 normalized TOF (10^{-6} mg^{-1} h^{-1} L)	Ref.

30AgINIF	TC- 10mg/L, Catalyst- 0.1mg in 3ml of TC solution, Time- 100 min, Light source- Cool white LED, H_2O_2-16.13 mM	99.23%	401.9 μmol g^{-1} h^{-1}	24.92	This work
Fe-g-C_3N_4/Bi_2WO_6	TC- 10mg/L, Catalyst- 0.4g/L, Time- 120 min, Light Source- Xenon lamp, H_2O_2-1mM	93.90%	10.57 μmol g^{-1} h^{-1}	10.57	[296]
$MnFe_2O_4$-Au	TC- 20mg/L, Catalyst- 0.1g/L, Time- 90min, Light source- Xenon lamp (300W), H_2O_2-50mM	88.3%	264.91 μmol g^{-1} h^{-1}	5.30	[297]
$MnFe_2O_4$/bio-char	TC-40mg/L, Catalyst- 0.5g/L, Time- 90 min, light source- Xenon lamp (300W), H_2O_2-100mM	93%	111.603 μmol g^{-1} h^{-1}	1.12	[298]
Ce_4O_7 modified Bi_4MoO_9	TC-10mg/L, Catalyst- 0.4g/L, Time- 300min, Light source-	95.32%	28.07 μmol g^{-1} h^{-1}	9.36	[299]

	5W white LED, H_2O_2-3mM				
(FeNi-LDH)/Ti_3C_2	TC- 20mg/L, Catalyst -0.2g/L, Time- 90 min, Light source- 300W xenon lamp, H_2O_2-20mM	94.7%	142.055 μmol g^{-1} h^{-1}	7.11	[300]
Fe doped porous carbon nitride	TC-100ml of 20g/L, Catalyst-0.5g/L, Time-80min, Light source- 300W xenon lamp, H_2O_2 -80mM	90.3%	66.970 μmol g^{-1} h^{-1}	0.84	[301]
TiO_2 coated α-Fe_2O_3 core shell	TC-200ml of 50mg/L, Catalyst-0.5g/L, Time-90min, Light source-300W xenon lamp, H_2O_2-5.871mM	100%	138.630 μmol g^{-1} h^{-1}	23.62	[302]
Fe/g-C_3N_4/kaolinite composite	TC- 65ml of 20 ppm, Catalyst-50mg, Time-80min, Light source- 500W xenon lamp, H_2O_2-1mM	88.1%	35.724 μmol g^{-1} h^{-1}	35.73	[303]

Oxygen vacancy and carbon doped $ZnFe_2O_4$	TC-20mg/L, Catalyst-0.5g/L, Time- 50min, Light source-300W xenon lamp, H_2O_2-10mM	90.8%	90.630 μmol g^{-1} h^{-1}	9.06	[304]
Cu@MoS_2/poly acrylamide/ Copper alginate nanocomposite double network	TC-50ml of 200ppm, Catalyst-50mg, Time-180min, Light source-300W xenon lamp, H_2O_2-1.5mM	90%	124.760 μmol g^{-1} h^{-1}	83.17	[305]

The possibility of metal ion leaching during photo Fenton experiments was investigated using Agilent 7800 ICP mass spectrometer. The ICP results show that the leaching of Fe, Ni metal ions after photo-Fenton degradation at pH 3 was ~0.30 %, and ~0.29 %, (of the 30AgINIF photocatalyst sample) respectively. Only 0.23% Ni leached out from the 30AgINIF sample after the neutral pH experiment. Ag metal leaching was negligible after photo Fenton degradation at both pH 3 and 7. Moreover, metal leaching at pH 7 is lesser than that observed at pH 3. so metal ion leaching cannot be main cause of reduced photo-Fenton activity at pH 7. Overall, metal leaching during the experiment at pH 3 and 7 are negligible or at a level which cannot affect tetracycline degradation to any significant extent [306–308]. Moreover, at neutral or higher pH, H_2O_2 can decompose into water and oxygen, reducing its availability to react with Fe^{2+} to produce ·OH[248].

Active species trapping experiments were carried out using EDTA and isopropyl alcohol (IPA). The EDTA behaves as h^+ species scavenger, while IPA acts as a hydroxyl radical scavenger[309,310]. Without scavenging agent, the tetracycline degradation efficiency of 30AgINIF catalyst was almost 100% in 100 min of the photo-Fenton reaction. In compare to this, when EDTA and IPA were added as scavenger in the reaction mixtures (TC+30AgINIF+H_2O_2) individually, the photodegradation efficiency was decreased by 89.2% and 77% respectively (Figure 7.10a). This implies, both species hydroxyl radical and h^+ actively involved in the photo-Fenton degradation of tetracycline.

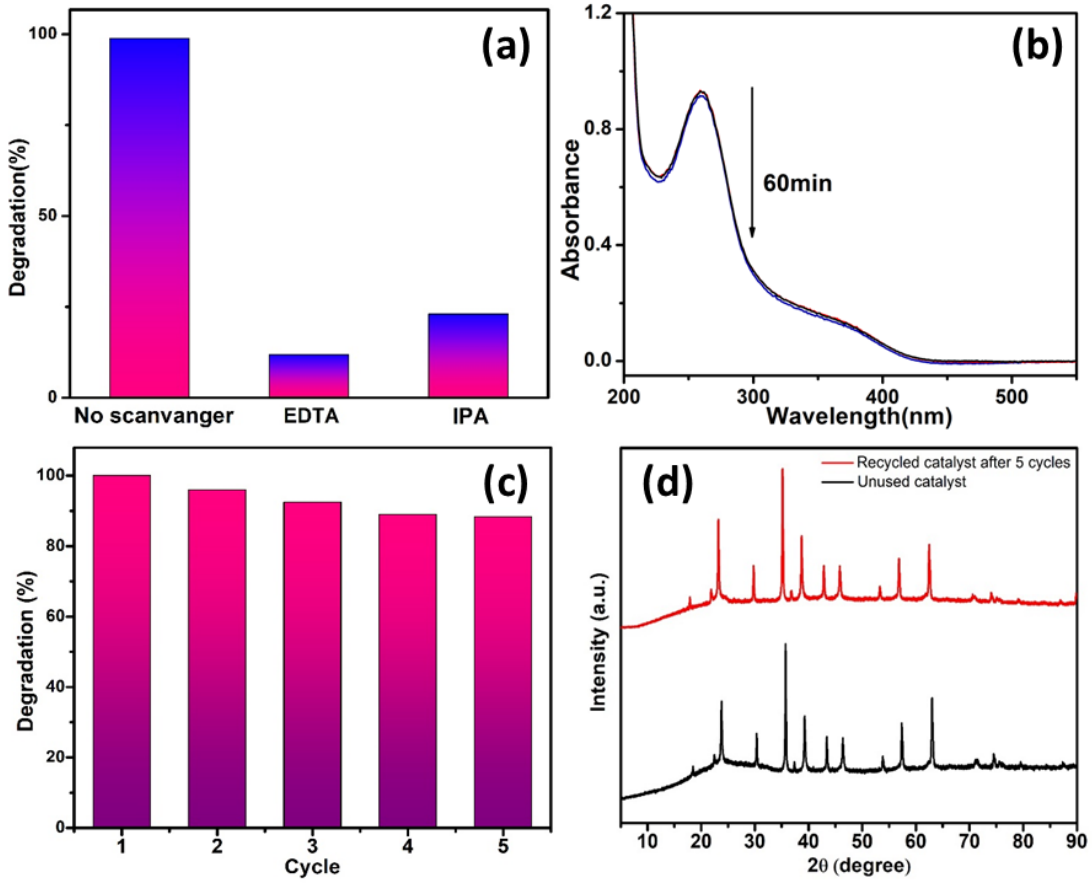

Figure 7.10 (a) Scavenger test, and (b) NBT test for TC degradation on 30AgNIF nanocomposite, (c) Recyclability test of 30AgINIF composite, and (d) XRD patterns of unused and recycled catalyst (30AgINIF) after 5 cycles. (Reaction conditions for UV-

Visible measurements- Concentration of TC- 10ppm, pH-3, H_2O_2 added- 100µl of 0.5M, and optical path- 10mm)

Moreover, the presence of superoxide radicals in the aqueous solution of the 30AgINIF photocatalyst was determined by utilizing the Nitroblue tetrazolium (NBT) test[311]. In a standard procedure, 100 microliters of the dispersed photocatalyst nanoparticles (1 mg/ml) were introduced into a quartz cuvette containing 3 ml of a NBT solution with a concentration of 2.5×10^{-5} mol/L. At regular time intervals, the photocatalyst was magnetically separated, and the resulting supernatant was subjected to analysis by UV-visible absorbance spectroscopy. The absence of any alteration in the absorption maxima of the NBT molecule at ~265 nm confirms that the superoxide radical ($\bullet O_2^-$) does not serve as an active species in the degradation process of TC molecules (Figure 7.10b).

Targeting the practical utilization of AgI/$NiFe_2O_4$ nanocomposites for TC photodegradation, photocatalytic recycling tests were conducted under visible-light irradiation, involving five successive and simultaneous conditions. For recyclability experiments. Initially, 6 mg of the catalyst was added to the 30 ml solution containing 10 ppm TC at pH 3 and sonicated. The mixture was placed in the dark for 30 minutes to attain adsorption-desorption equilibrium. Afterwards, an appropriate amount of 0.5 M H_2O_2 was added to the reaction mixture. Thereafter, the mixture was placed under the cool white LED visible light. After every cycle, the catalyst was magnetically collected, washed thoroughly with distilled water, and dried in a hot air oven. Figure 7.10c illustrates the reusability of 30AgINIF via consecutive experiments (5 cycles). The photo-Fenton degradation efficiency of photocatalyst was ~89% after 5 cycles. Additionally, the prepared photocatalyst demonstrated easy separation for reuse with an external magnet. Figure 7.10d compares the XRD patterns of unused 30AgINIF and recycled 30AgINIF. All XRD peaks

of the recycled 30AgINIF match well with that exhibited by the fresh sample, demonstrating the stability of the former.

7.3.3 DFT calculations

Figure 7.11 displays the NIF30_AgI5 composite model's simulated absorption spectra. The vertical lines depict the excitations associated with electronic transitions at different wavelengths. The solid black curve in the same figure displays the experimental solid-state UV-visible spectrum of the 30AgINIF composite. Ground and excited state HOMO and LUMO locations were determined on the NIF30_AgI5 structure (Figure 7.12). The excited state HOMO-LUMO analysis was implemented on the 599 nm (Figure 7.11) excited state. In the ground state, the HOMO is mainly on the AgI cluster and partially on $NiFe_2O_4$ cluster, while the LUMO is predominantly on the AgI part. The HOMO shifted from the AgI cluster to Fe and O atoms of the $NiFe_2O_4$ unit after photoexcitation. Thus, photoexcitation transfers charge from the AgI portion to the $NiFe_2O_4$ part and makes the latter a nucleophilic region.

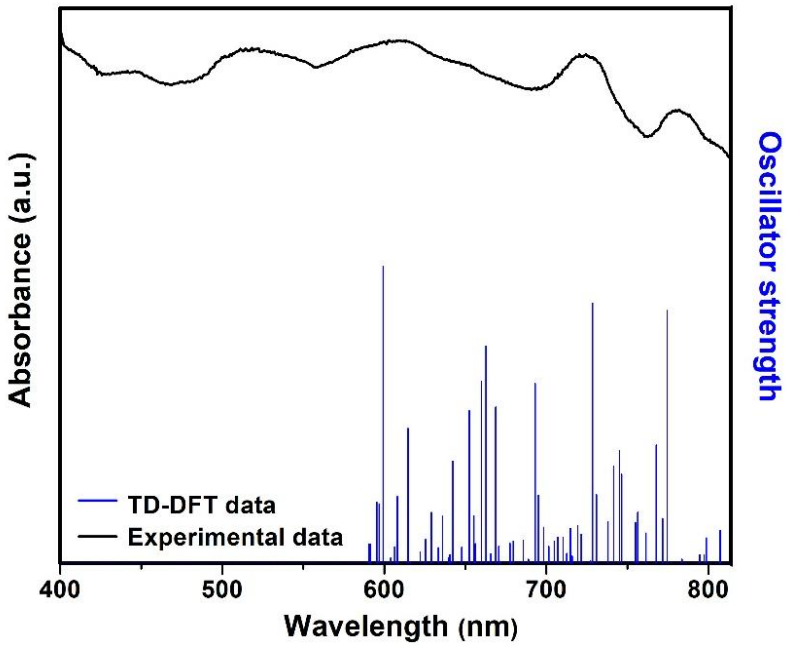

Figure 7.11 Solid-state UV-visible absorption spectrum of 30AgINIF composite (solid black curve) and TD-DFT calculated UV-visible absorption spectrum of NIF30_AgI5 model (blue).

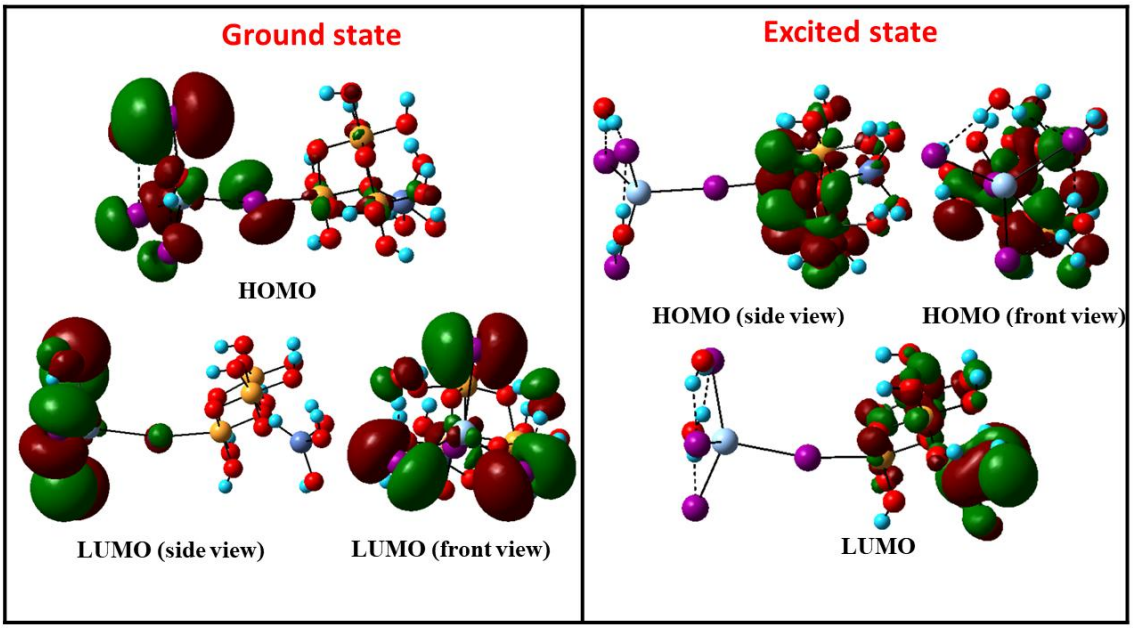

Figure 7.12 HOMO/LUMO (excited state (599 nm) and ground state) calculated using DFT and TDDFT methods.

Separate DFT calculations were carried out to investigate the interaction of H_2O_2 with $NiFe_2O_4$ and AgI parts in the ground and excited state NIF30_AgI5. The optimized H_2O_2 interaction conformations are henceforth abbreviated as NIF30_AgI5_H_2O_2 (*H_2O_2 interacts with the AgI part*), and H_2O_2-NIF30_AgI5 (*H_2O_2 interacts with the $NiFe_2O_4$ part*) systems. Figure 7.13a and 7.13b display the H_2O_2 interaction conformations respectively with AgI and the $NiFe_2O_4$ parts of the excited state NIF30_AgI5 structure. The interaction energies of H_2O_2 with the AgI and $NiFe_2O_4$ parts of NIF30_AgI5 system have been investigated on the basis of HOMO-LUMO locations in the ground state and excited states. The interaction energies of H_2O_2_NIF30_AgI5 and NIF30_AgI5_H_2O_2 systems have been calculated using equations 7.1, and 7.2,

$$E_{interaction} = E_{(H2O2\_NIF30\_AgI5)} - [\, E_{(NIF30\_AgI5)} + E_{(H2O2)}] \quad (7.1)$$

$$E_{interaction} = E_{(NIF30\_AgI5\_H2O2)} - [\, E_{(NIF30\_AgI5)} + E_{(H2O2)}] \quad (7.2)$$

In equations 7.1, and 7.2, 'E' represents the potential energy of the respective molecular system.

Table 7.2 displays the details of the H_2O_2 interaction potential energy calculations of various NIF30_AgI5-H_2O_2 models. Only the interaction of H_2O_2 with $NiFe_2O_4$ part of NIF30_AgI5 system in excited state gives a negative interaction energy. In case of NIF30_AgI5_H_2O_2 system, the interaction of H_2O_2 with AgI part of the excited state NIF30_AgI5 system demonstrates a small positive interaction energy. The interaction energies are positive for the interaction of H_2O_2 with $NiFe_2O_4$ and AgI parts of the ground state NIF30_AgI5 system.

Figure 7.13(a) shows that the O atom of H_2O_2 interacts with Ag atom of AgI part, while one of the H atoms of H_2O_2 interacts with I atom of AgI part in NIF30_AgI5_H_2O_2 system. In the H_2O_2_NIF30_AgI5 system (Fig. 7.13b) the O atom of H_2O_2 molecule bonds with Fe atom of $NiFe_2O_4$ part, while one of the H atoms of H_2O_2 interacts with the lattice O of the $NiFe_2O_4$. This indicates that H_2O_2 prefers to interact with the Fe atom of the $NiFe_2O_4$ part in excited state. Figure 7.14(a-c) exhibits the structural details of these two H_2O_2 interaction systems with the optimized structure of the isolated H_2O_2 molecule. The O_α – O_β bond lengths in NIF30_AgI5_H_2O_2 and H_2O_2_NIF30_AgI5 systems are 1.566 Å and 1.691 Å respectively. The longer O_α – O_β bond length in the H_2O_2_NIF30_AgI5 system implies greater bond activation and weakening of the O-O bond of H_2O_2 molecule.

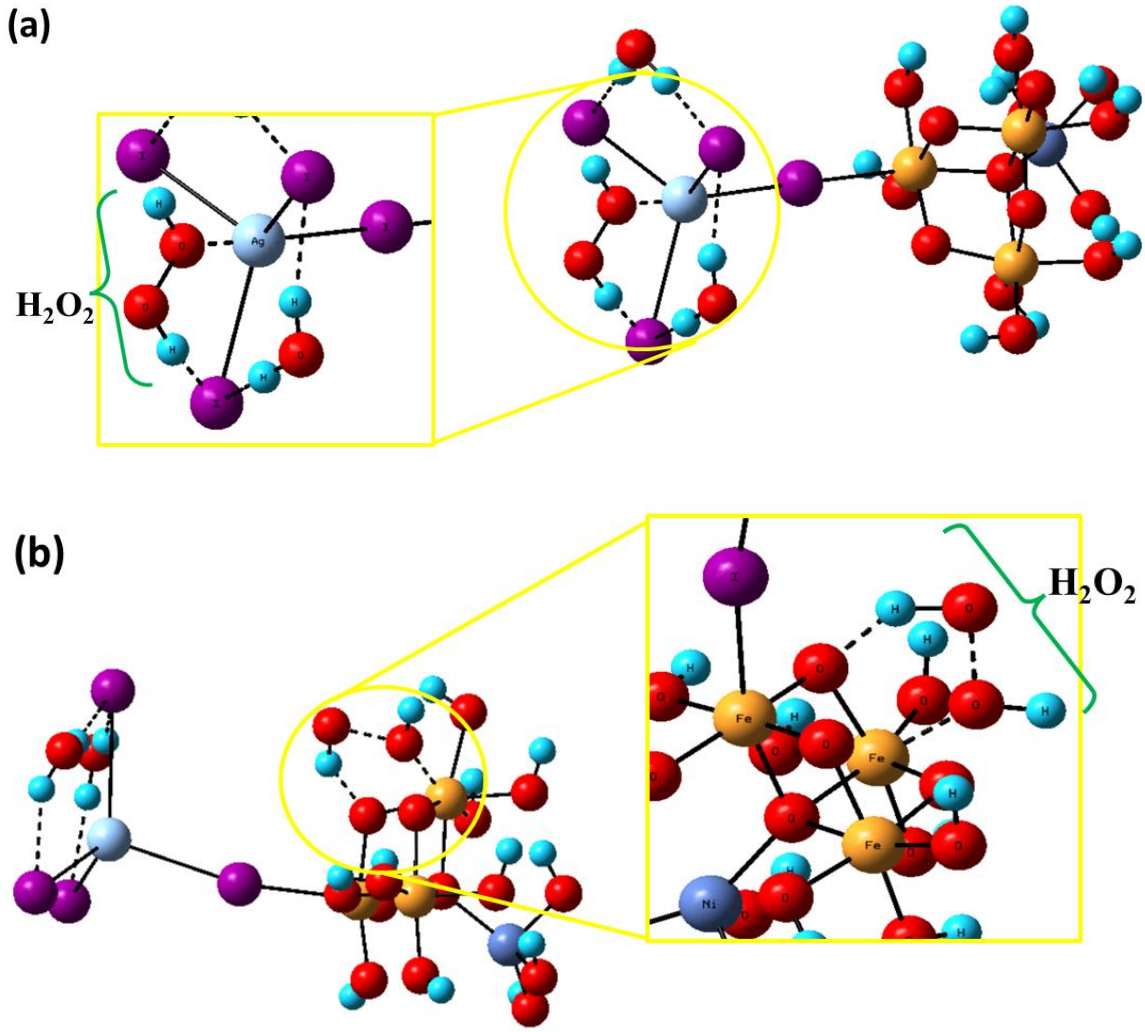

Figure 7.13 The interaction structure of (a) NIF30_AgI5_H_2O_2, and (b) H_2O_2-_NIF30_AgI5 systems.

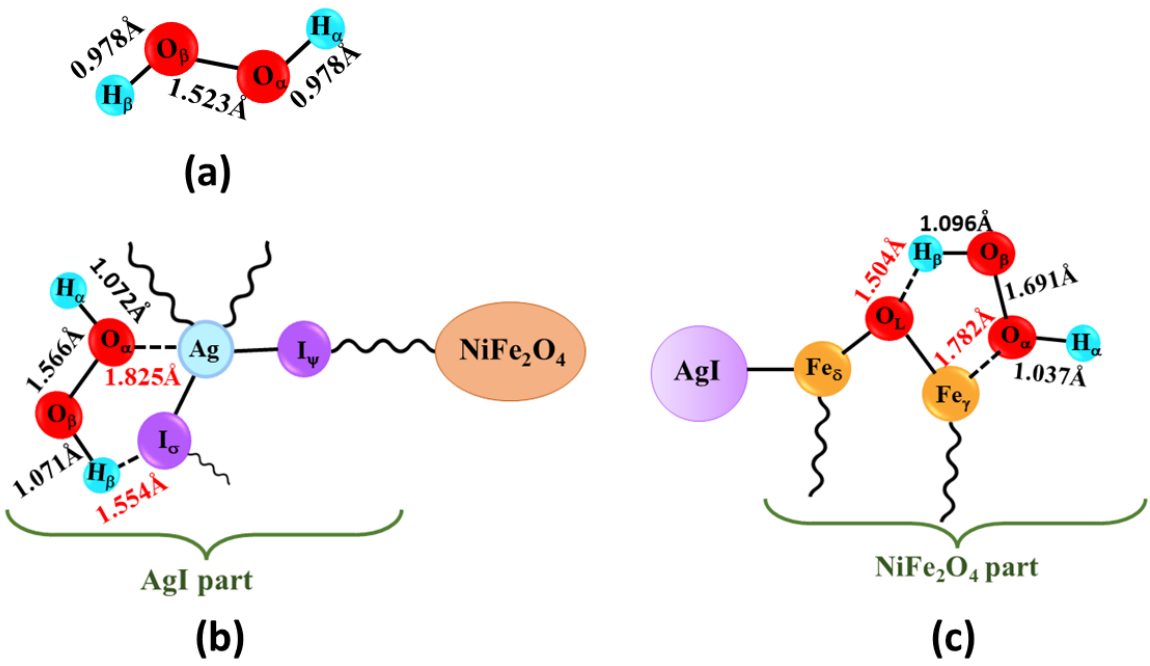

Figure 7.14 Interaction/bond lengths in (a) optimized H_2O_2 molecule, (b) NIF30_AgI5_H_2O_2, and (c) H_2O_2-NIF30_AgI5 systems. Different symbols have been used to denote atom types in the H_2O_2, NIF30_AgI5 system.

Table 7.2 presents the potential energies of molecules, composite and composite- H_2O_2 interaction models. (Where, 1 Hartree = 27.21eV)

System	Potential energy (Hartree)	Interaction energy (Hartree)
H_2O_2	-151.546	
NIF30_AgI5	-39465.251	
H_2O_2_NIF30_AgI5 (ground state)	-39616.730	0.066
H_2O_2_NIF30_AgI5 (excited state)	-39616.871	-0.075
NIF30_AgI5_H_2O_2 (excited state)	-39616.664	0.130
NIF30_AgI5_H_2O_2 (ground state)	-39616.497	0.30

NBO calculations were performed on optimized models of H_2O_2-catalyst interactions in the excited state, utilizing single-point calculations at the same level of theory (table 7.3). The

second-order stabilization energy $E^{(2)}$, assessed through NBO analysis, arises from electron delocalization concerning the corresponding natural Lewis structure. Quantification of the delocalization adjustments to the zeroth-order natural Lewis structure is achieved by observing higher $E^{(2)}$ values [239,241]. Equation (7.3) employs second-order perturbation theory to calculate this energy $E^{(2)}$.

$$E^{(2)} = q_i \frac{(F_{i,j})^2}{(\varepsilon_j - \varepsilon_i)}, \qquad (7.3)$$

In equation (7.3), q_i = donor orbital occupancy, ε_i = energy of accepter NBO, ε_j = energy of donar NBO, $F_{i,j}$ =off diagonal Fock matrix element.

Table 7.3 The delocalization energy ($E^{(2)}$ in kcal/mol) analysis of charge transfer from donor to acceptor NBO of the H_2O_2_NIF30_AgI5 and NIF30_AgI5_H_2O_2 systems. In the table, "LP" indicates the 1-center nonbonding lone pair electrons, "LP*" signifies a 1-center vacant orbital, "BD" abbreviates 2-center bonding (σ) orbital, and "BD*" represents a 2-center antibonding σ* orbital[240].

System	Donor NBO	Acceptor NBO	$E^{(2)}$(kcal/mol)
H_2O_2_NIF30_AgI5	LP (O_α)	BD*(Fe_γ–O_L)	20.54
	BD (O_α – O_β)	LP*(Fe_γ)	22.51
	LP (Fe_γ)	BD*(O_α – O_β)	84.77
	LP (O_L)	BD*(O_β– H_β)	16.73
NIF30_AgI5_H_2O_2	LP (Ag)	BD*(O_α – O_β)	10.74
	BD (Ag – I_ψ)	BD*(O_α– O_β)	1.90
	BD (O_α – O_β)	LP*(Ag)	4.00
	LP (I_σ)	BD*(I_σ – H_β)	1.29

In the H_2O_2-NIF30_AgI5 system, charge transfer takes place from LP (O_α) to BD*(Fe_γ–O_L) orbital with 20.54 kcal/mol stabilization energy. Similarly, the BD (O_α – O_β) to LP*(Fe_γ) charge transfer has 22.51 kcal/mol stabilization energy. These transfers increase charge density on the Fe centre. Naturally, a strong donation occurs from LP (Fe_γ) to BD*(O_α –

O_β) orbital with 84.77 kcal/mol delocalization energy. This causes the weakening of the O_α – O_β bond due to increased electron density in its antibonding orbital and decreased electron density in its bonding orbital. Furthermore, the weakening of the Fe_γ-O_L bond (due to charge transfer to its antibonding orbital) facilitates a delocalization from LP(O_L) to BD*(O_β– H_β) orbital (~16.73 kcal/mol $E^{(2)}$ value). This hydrogen bonding between hydrogen of H_2O_2 and lattice oxygen atom of nickel ferrite part weakens the O_β– H_β bond. In contrast the NIF30_AgI5_H_2O_2 system, demonstrates a weaker LP(Ag) towards BD*(O_α – O_β) orbital delocalization with 10.74 kcal/mol stabilization energy. There is also a charge transfer from donor BD (Ag – I_ψ) orbital to the acceptor BD*(O_α – O_β) with an $E^{(2)}$ of 1.90 kcal/mol. At the same time a back donation takes place from BD (O_α – O_β) to LP*(Ag) orbital having $E^{(2)}$ value 4.00 kcal/mol. A LP (I_σ) to BD*(I_σ – H_β) orbital delocalization also takes place with 1.29 kcal/mol stabilization energy. The $E^{(2)}$ values of all NIF30_AgI5_H_2O_2 interactions are much lesser than observed for the H_2O_2-NIF30_AgI5 system. Clearly H_2O_2 interaction with nickel ferrite is much stronger than with AgI part in the NIF30_AgI5 system.

7.4 Photo-Fenton mechanism

Figure 7.15 presents a plausible photocatalytic photo-Fenton mechanism based on the experimental and theoretical findings mentioned earlier. Mott-Schottky and solid-state UV-DRS measurements show that the band gaps of AgI and $NiFe_2O_4$ components of the composite are staggered relative to each other. The Nyquist plot results give the effective charge transfer kinetics. Thus, visible light irradiation excites electrons from the VB to the CB of AgI and $NiFe_2O_4$ parts of the 30AgINIF composite. TD-DFT calculations shows electron transfer due to photoexcitation from the AgI to the $NiFe_2O_4$ part of the composite, implying a Z-scheme type mechanism (Eq. 7.4). Especially, the excited HOMO is located

on the Fe-centres of the $NiFe_2O_4$ part of the composite (Eq. 7.5). The NBO calculations show that the electron-rich Fe-centres of $NiFe_2O_4$ react with H_2O_2, activating the HO-OH bond, leading to the production of •OH (Eq. 7.6). These hydroxyl radicals then oxidize TC to small aliphatic fragments. Equations 7.4 to 7.8 depict the sequence of chemical events that may be taking place during the photo-Fenton TC degradation on AgI/$NiFe_2O_4$ composite.

$$AgI/NiFe_2O_4 + hv \rightarrow NiFe_2O_4\,(e^- + h^+) \quad (7.4)$$

$$Fe^{3+} + e^- \rightarrow Fe^{2+} \quad (7.5)$$

$$Fe^{2+} + H_2O_2 \rightarrow Fe^{3+} + \bullet OH + OH^- \quad (7.6)$$

$$h^+_{VB} + H_2O/\,OH^- \rightarrow H^+ + \bullet OH \quad (7.7)$$

$$\bullet OH + tetracyline \rightarrow degradation\ products \quad (7.8)$$

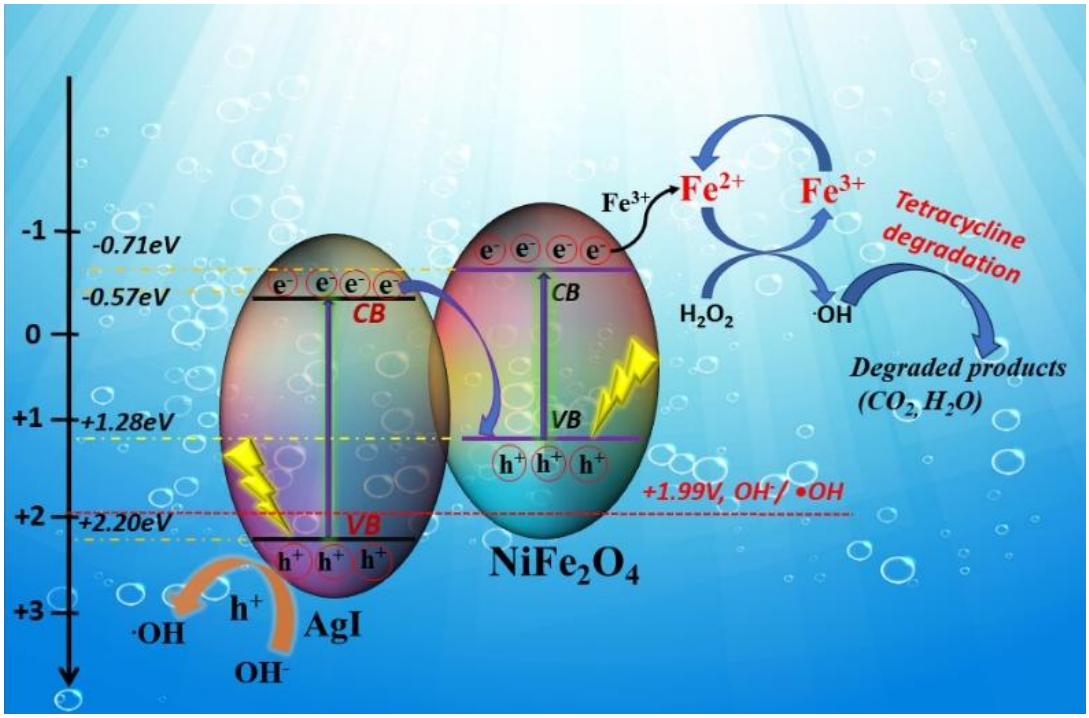

Figure 7.15 Schematic Z-scheme mechanism for photo-Fenton degradation of TC on AgI/$NiFe_2O_4$ nanocomposite.

7.5 Conclusions

Parameters such as light absorption, band positions, band gaps, and magnetic properties enabled us to shortlist AgI/$NiFe_2O_4$ as a possibly effective photo-Fenton photocatalyst. DFT and TD-DFT calculations showed that in the ground state the HOMO of the composite is primarily on AgI, while the excited state HOMO is predominantly on the $NiFe_2O_4$ part. The HO-OH bond (in H_2O_2) showed maximum activation when H_2O_2 interacted with the $NiFe_2O_4$ part of the model of the composite. Overall, DFT and TD-DFT calculations suggested charge transfer from the AgI to the $NiFe_2O_4$ side on photoexcitation to enable efficient interaction between the Fe part (of the $NiFe_2O_4$ side) and H_2O_2 for hydroxyl radical production.

Based on these preliminary DFT predictions, three AgI/$NiFe_2O_4$ composites with varying percentage of AgI were prepared by a two-step precipitation process. The resulting photocatalysts exhibited remarkable tetracycline photo-Fenton degradation activities. Nyquist plot analysis established that the 30-weight percent AgI loading on $NiFe_2O_4$ composite has best the charge transfer kinetics among those studied in this research. The optimum TC degradation photo-Fenton activity was observed on the 30AgINIF composite, and its TOF value is significantly higher than earlier reports on other photocatalysts. The superparamagnetic composite demonstrated easy magnetic separation and proficient reusability for photo-Fenton TC degradation. A combination of DFT calculations and experimental observations suggest the operation of a Z-scheme photocatalytic mechanism.